Structural and magnetic study of $Tb_{1-x}Ca_xMnO_3$ perovskites

J. Blasco,[1] C. Ritter,[2] J. García,[1] J. M. de Teresa,[1] J. Pérez-Cacho,[1] and M. R. Ibarra[1]
[1]*Instituto de Ciencia de Materiales de Aragón and Departmento de Física de la Materia Condensada, Consejo Superior de Investigaciones Científicas y Universidad de Zaragoza, 50009 Zaragoza, Spain*
[2]*Institut Laue-Langevin, Boîte Postale 156, 38042 Grenoble Cédex 9, France*
(Received 7 February 2000)

The crystal and magnetic structures of $Tb_{1-x}Ca_xMnO_3$ series have been studied by x-ray and neutron-diffraction techniques. Macroscopic magnetic properties have been characterized using ac magnetic susceptibility measurements. The relationships between structural and magnetic behaviors are discussed. Our study shows that the magnetism of manganese in this system is very complex due to the small size of the rare earth. $TbMnO_3$ does not develop a simple *A*-type magnetic order, as does $LaMnO_3$, but an incommensurate sinewave structure. As the Ca content increases up to $x=0.33$, the magnetization increases without, however, reaching a truly ferromagnetic state. Instead, the magnetic ground state is composed of ferromagnetic clusters in a paramagnetic matrix. Charge ordering is observed at higher values of *x* and the magnetic ground state evolves, with increasing *x* values, from the *CE* type to a mixture of different magnetic structures including some noncollinear structures. For $x=0.85$, we observe a phase segregation at low temperatures into an orthorhombic phase and a monoclinic phase.

I. INTRODUCTION

Mixed oxides of rare earth and manganese were extensively studied in the past due to their magnetic properties.[1–3] These compounds show both, antiferromagnetic (AF) and ferromagnetic (F) interactions depending on the Mn^{3+}/Mn^{4+} ratio and the physics of manganites has primarily been described by the double exchange model.[1] However a current burst of activity has been stimulated by the discovery of giant magnetoresistance in some of these compounds[4] and the recent studies are pointing out to their great complexity. The $R_{1-x}A_xMnO_3$ (R=rare earth; A=Ba, Sr, Ca; hereafter denoted as *A*-site cations) compounds display a great variety of magnetic structures[2,5] and charge ordering phenomena.[6,7] The pioneering work of Wollan *et al.*[2] revealed different magnetic structures (*A*, *G*, *CE*, or *C* types) for these compounds. We refer the reader to this reference to get a full description of these magnetic structures.

Different effects such as the electron-phonon interaction,[8,9] the average size of the *A*-site cations,[10] and the mismatch between the *A*-site cations[11] modulate the physical properties of these compounds. So far, the light *R*-based compounds (La, Pr, or Nd) have been intensely investigated,[1–11] whereas fewer studies have concentrated on heavy *R*-based systems.[12,13] In particular, there is no published information about the evolution of the magnetic properties and the magnetic ground state for the $Tb_{1-x}Ca_xMnO_3$ system. The only available information corresponds to particular samples ($x=0.5$ and 0.33) studied by us in previous works.[14,15] This system is interesting because the Tb-based samples are close to the limit of stability for perovskite compounds and the resulting structure is very distorted (competitive hexagonal phase appears in $RMnO_3$ with R=Ho, Er, Tm, Yb, and Lu). This allows one to study the magnetic properties of manganites with a narrow one-electron bandwidth.

The aim of this work is to determine with accuracy the magnetic properties and magnetic ground state for this series in order to compare our results with the related systems. Our results are interpreted by considering the role of superexchange, double exchange and the small size of Tb^{3+} ions.

II. EXPERIMENTAL SECTION

A wide set of $Tb_{1-x}Ca_xMnO_3$ samples ($x=0$,0.15, 0.25,0.33,0.45,0.50,0.55,0.65,0.75,0.85,0.95,1) were prepared by solid state chemistry procedures. Stoichiometric amounts of Tb_4O_7, $CaCO_3$, and $MnCO_3$ with nominal purities not less than 99.99% were mixed, ground and calcined overnight at 950 °C. Then, they were ground, pressed at 7 kbar and sintered at 1250 °C in air for 3 days with intermediate grindings. Finally, samples with $x<0.25$ and with $x>0.5$ were annealed overnight at 1000 °C in nitrogen and oxygen current flows, respectively, in order to optimize the oxygen content.

The oxygen content was determined by means of redox titration and the results of the analysis are summarized in Table I together with the chemical composition of the samples. All samples can be considered stoichiometric within the experimental error. Consequently, the effects arising from oxygen or cation vacancies must be negligible.

X-ray diffraction patterns were collected using a Rigaku D/max-B instrument with a copper rotating anode and a graphite monochromator to select the CuK_α wavelength. The device was working at 40 kV and 100 mA. In order to perform Rietveld analysis, some selected samples were measured in step-scanned mode from $18° \leqslant 2\theta \leqslant 140°$ in steps of 0.02° with a counting rate of 8 s/step. A continuous-helium-flow cryostat from Oxford Instruments was coupled to the goniometer in order to measure at different temperatures down to 15 K. In this case the device was working at 45 kV and 160 mA. Neutron-diffraction experiments were carried out at different temperatures at the high-flux reactor of the ILL using the D1B instrument and working with a wavelength of 2.52 Å covering an angular range $2° \leqslant 2\theta \leqslant 100°$. Structural refinements were made of both, x-ray and neutron

TABLE I. Nominal composition, Mn^{4+} content obtained by redox titration and the atmosphere of synthesis for the $Tb_{1-x}Ca_xMnO_3$ series.

Nominal composition	Mn^{4+} (%)	Sintering conditions
$TbMnO_3$	3	air+N_2 annealing
$Tb_{0.85}Ca_{0.15}MnO_3$	16	air+N_2 annealing
$Tb_{0.75}Ca_{0.25}MnO_3$	27	air
$Tb_{0.67}Ca_{0.33}MnO_3$	34	air
$Tb_{0.55}Ca_{0.45}MnO_3$	47	air
$Tb_{0.5}Ca_{0.5}MnO_3$	49	air
$Tb_{0.45}Ca_{0.55}MnO_3$	55	air+O_2 annealing
$Tb_{0.35}Ca_{0.65}MnO_3$	66	air+O_2 annealing
$Tb_{0.25}Ca_{0.75}MnO_3$	77	air+O_2 annealing
$Tb_{0.15}Ca_{0.85}MnO_3$	86	air+O_2 annealing
$Tb_{0.05}Ca_{0.95}MnO_3$	92	air+O_2 annealing
$CaMnO_3$	96	air+O_2 annealing

diffractograms, by using the FULLPROF program.[16]

Magnetic measurements were carried out between 5 and 300 K by using a commercial Quantum Design (SQUID) magnetometer with an ac experimental setup. Measurements of magnetic ac susceptibility were performed at frecuencies ranging from 1.2 to 120 Hz and an amplitude of the oscillating magnetic field of 4.5 Oe. All samples studied in this work are semiconducting or insulating and the electrical conductivity at room temperature decreases with increasing Tb content.

III. RESULTS

A. Crystal structure at room temperature

The analysis of the x-ray diffraction patterns indicates single-phase compounds for all $Tb_{1-x}Ca_xMnO_3$ samples at room temperature. Observed diffraction peaks can be indexed in the orthorhombic *Pbnm* space group (standard setting *Pnma*, No. 62). This is one of the most common distorted structures derived from the cubic perovskite. Rietveld profile analysis was performed for selected samples and the results are summarized in Table II. This analysis was also carried out for $x=0.33$ and $x=0.5$ samples but their results have been already reported[14,15] and we will refer to these references in order to compare our results. Table III shows the Mn-O distances and ⟨Mn-O-Mn⟩ bond angles obtained from the refined atomic positions together with the MnO_6 octahedron distortion for each sample. For the sake of clarity, we have included the data for $x=0.33$ and $x=0.5$ samples. The lattice parameters obtained for both end-members of the series nicely agree with the data reported previously.[17,18] The unit cell volume decreases with increasing Ca content reflecting the large difference in the ionic radii between[19] Mn^{3+} and Mn^{4+} that overcomes the difference between Ca^{2+} and Tb^{3+}. Figure 1 shows the evolution at room temperature of both, lattice parameters and unit cell volume, along the series. $TbMnO_3$ shows a large orthorhombic distortion indicated by the large differences between the *a* and *b* lattice parameters. This is the macroscopic mark of the cooperative Jahn-Teller distortion due to the Mn^{3+} ion in an octahedral environment (see Table III). Both, the orthorhombic and the octahedron distortion decrease with increasing the Ca content (see Fig. 1 and Table III) and the other end member $CaMnO_3$, with Mn^{4+} and regular MnO_6 octahedra shows a nearly cubic unit cell. Therefore, the *b* axis decreases strongly with increasing Ca content while the other lattice parameters have singular features as can be observed in Fig. 1. The lack of a continuous evolution in these lattice parameters indicates the large correlation between the electronic state of Mn atoms and the geometrical structure of the unit cell. The *a*-axis peaks at $x=0.5$ while the *c* axis has a

TABLE II. Fractional atomic coordinates and isotropic thermal factors for *R*(Tb/Ca), Mn and O atoms (note that an average thermal factor has been considered for both kind of oxygen atoms). Lattice parameters and reliability factors (unweighted, weighted, χ^2 and Bragg) defined as in Ref. 16. Numbers in parentheses indicates standard deviations of the last digits. Data for $x=0.33$ and $x=0.5$ samples have already been reported in Refs. 14 and 15.

	$x=0$	$x=0.15$	$x=0.25$	$x=0.75$	$x=0.85$	$x=1$
R:x	0.9836(1)	0.9841	0.9853(2)	0.9920(3)	0.9905(3)	0.9929(4)
y	0.0810(1)	0.0724	0.0645(1)	0.0399(1)	0.0369(1)	0.0313(1)
B (Å^2)	0.84(1)	0.86(3)	0.81(4)	0.64(2)	0.71(1)	0.52(1)
O(1):x	0.1083(8)	0.1112(12)	0.1042(10)	0.0750(10)	0.0657(7)	0.0624(8)
y	0.4694(8)	0.4768(12)	0.4676(6)	0.4843(6)	0.4869(5)	0.4869(5)
B (Å^2)	0.94(7)	0.42(9)	0.61(5)	1.20(5)	1.31(4)	0.89(3)
O(2):x	0.7085(7)	0.7093(10)	0.7088(11)	0.7062(7)	0.7093(5)	0.7118(6)
y	0.3267(6)	0.3056(9)	0.3015(9)	0.2861(7)	0.2877(5)	0.2882(6)
z	0.0523(4)	0.0465(7)	0.0466(7)	0.0360(5)	0.0349(4)	0.0342(4)
B (Å^2)	0.94(7)	0.42(9)	0.61(5)	1.20(5)	1.31(4)	0.89(3)
Mn:B (Å^2)	0.75(2)	0.63(4)	0.77(4)	0.25(2)	0.23(1)	0.14(1)
a (Å^2)	5.3019(1)	5.3076(2)	5.3180(3)	5.3049(2)	5.2824(1)	5.2687(1)
b (Å)	5.8557(1)	5.6962(3)	5.5997(4)	5.3529(2)	5.3133(1)	5.2813(1)
c (Å)	7.4009(1)	7.4547(3)	7.4879(5)	7.4805(5)	7.4731(1)	7.4582(1)
R_p/R_{wp} (%)	5.3/7.7	7.5/9.7	7.4/9.4	4.8/6.8	5.0/6.8	6.0/8.9
χ^2	3.1	3.8	3.9	2.8	2.3	2.6
R_{Bragg} (%)	4.2	4.1	4.4	2.9	3.2	2.5

TABLE III. Interatomic Mn-O distances (Å), octahedron distortion and angles (deg.) between the MnO_6 octahedra for $Tb_{1-x}Ca_xMnO_3$ samples obtained from refined atomic positions at room temperature. The octahedron distortion is defined as $D_{oct}=10\times(\Sigma|(\text{Mn-O}i)-\langle\text{Mn-O}\rangle_{average}|)/\langle\text{Mn-O}\rangle_{average}$.

No.	$x=0$	$x=0.15$	$x=0.25$	$x=0.33$	$x=0.5$	$x=0.75$	$x=0.85$	$x=1$
Mn-O(1): 2	1.946(1)	1.959(2)	1.961(2)	1.957(2)	1.940(4)	1.914(1)	1.901(1)	1.895(1)
Mn-O(2): 2	2.243(4)	2.094(5)	2.051(5)	2.009(5)	1.965(12)	1.901(4)	1.905(3)	1.904(3)
2	1.889(4)	1.931(5)	1.938(5)	1.949(5)	1.948(12)	1.952(4)	1.923(3)	1.903(3)
$\langle\text{Mn-O}\rangle_{average}$	2.026	1.995	1.983	1.979	1.951	1.922	1.910	1.901
D_{oct}	2.14	0.99	0.68	0.38	0.14	0.30	0.14	0.06
Mn-O(1)-Mn:								
2	143.98(6)	144.04(9)	145.41(9)	146.6(3)	149.0(2)	155.46(5)	158.54(3)	159.57(3)
Mn-O(2)-Mn:								
4	145.7(1)	150.6(2)	151.0(2)	151.6(8)	154.2(5)	155.8(1)	156.3(1)	156.8(1)
$\langle\text{Mn-O-Mn}\rangle_{av}$	145.1	148.4	149.1	149.9	152.5	155.7	157.0	157.7

local minimum at this composition. These features must be related to the charge-ordering structure along the ac plane shown by this sample[14] at 300 K. Its real unit cell is monoclinic although it is hard to notice superstructure peaks at room temperature. The *c*-axis peaks at $x=0.33$ at which the related compounds, as $La_{2/3}Ca_{1/3}MnO_3$, show the highest temperature of ferromagnetic transition. Ferromagnetic interactions are also present in $Tb_{2/3}Ca_{1/3}MnO_3$ as evidences its spin-glass-like behavior at low temperatures.[15] In addition, the replacement of Tb by Ca also affects the bond angles between neighboring octahedra (see Table III). These angles are very low for $TbMnO_3$ due to the low Tb^{3+} ion size, and they increase with increasing Ca content.

B. Structural and magnetic properties below room temperature

Neutron-diffraction experiments were performed on selected samples ($x=0$, 0.15, 0.33, 0.5, 0.65, and 0.85) in order to study both, the thermal evolution and the magnetic ground state. First, we present the structural data and, subsequently, we correlate these data with macroscopical magnetic measurements.

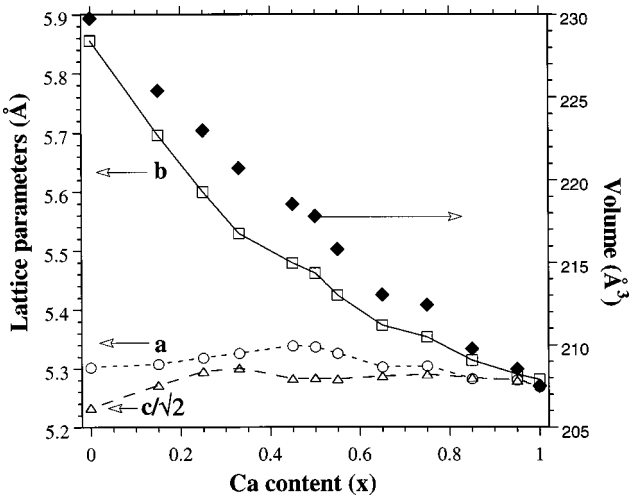

FIG. 1. Lattice parameters and unit cell volume for $Tb_{1-x}Ca_xMnO_3$ samples at room temperature.

1. Thermal evolution of the lattice parameters

All of these samples have been refined in the *Pbnm* space group at room temperature. Figure 2 shows the thermal evolution of the refined lattice parameters in this space group. Lattice parameters for $TbMnO_3$ and $Tb_{0.85}Ca_{0.15}MnO_3$ samples exhibit a similar thermal evolution with a slight decrease in both, *b* and *c* axes, with decreasing temperature. However, no changes are observed in the *a*-parameter, within the experimental error, down to 125 K. Below this temperature, a small increase in its value is noticed for both samples.

Small variations are observed in both, *a* and *b* axes, for $Tb_{0.67}Ca_{0.33}MnO_3$. Only the *c* axis decreases when lowering the temperature down to 200 K. On further cooling down it remains essentially constant down to 2 K. Large jumps are perceived in the thermal dependence of the lattice parameters at high temperatures for $Tb_{0.5}Ca_{0.5}MnO_5$ and $Tb_{0.35}Ca_{0.65}MnO_3$ compounds. While the *a* and *b* parameters increase with decreasing temperature, the *c* axis decreases, these variations being sharper for the $Tb_{0.5}Ca_{0.5}MnO_3$ sample. In this sample, these changes can be related to the formation of a charge ordered state at room temperature as reported elsewhere.[14] The ordering is established within the ac plane (considering the *Pnma* space group setting) and the observed superstructure peaks are consistent with a monoclinic unit cell $P2_1/m$ that can be obtained from the orthorhombic *Pnma* by doubling the *a* axis. The similar behavior observed in $Tb_{0.35}Ca_{0.65}MnO_3$ might suggest a similar charge ordering for this sample but in this case, we have not noticed any superstructure diffraction peak below the transition temperature and accordingly, an orthorhombic unit cell can account for the patterns down to 2 K. Later, we will show that in fact different magnetic ground states are observed for these two compositions.

Finally, a sharp change is perceived for all lattice parameters around 130 K in the $Tb_{0.15}Ca_{0.85}MnO_3$ sample. This is an indication of both, the phase transition and the phase segregation undergone by this compound.

2. Magnetic structures

Let us report now on the magnetic ground states and the magnetic transitions observed for these compounds. Figure 3 displays the Rietveld refinement of the neutron-diffraction spectra at 16 K of the $TbMnO_3$ sample. The Mn moments

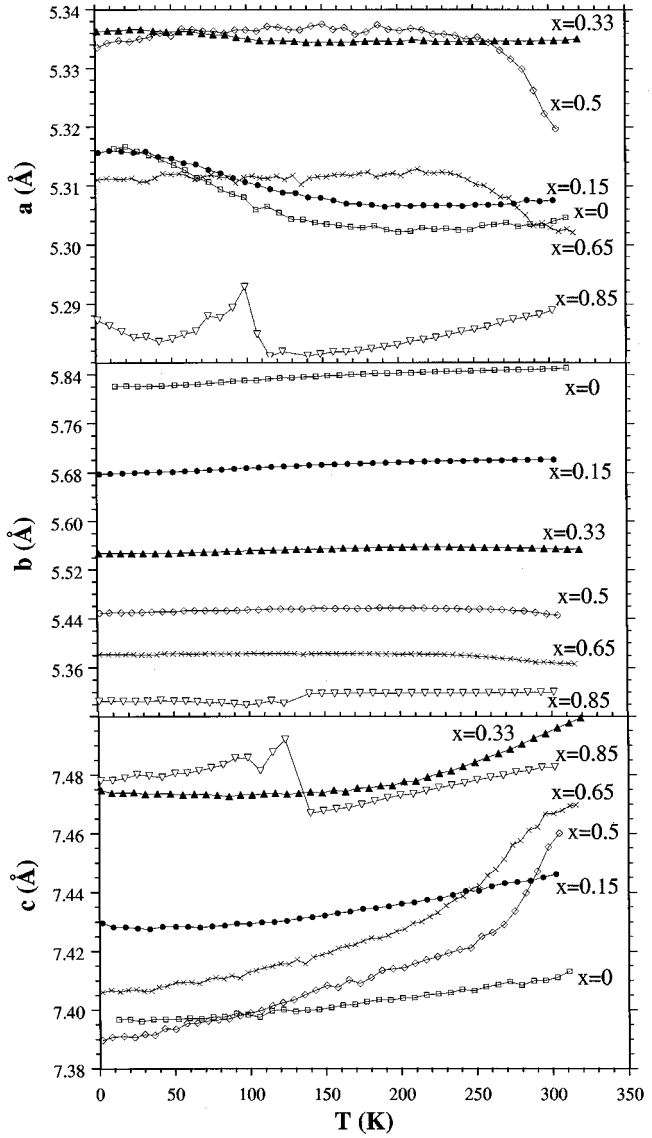

FIG. 2. Thermal evolution of the lattice parameters obtained from neutron diffraction data for selected $Tb_{1-x}Ca_xMnO_3$ samples. The values of x are displayed in the figure. Note: The orthorhombic phase is minority for $x=0.85$ at low temperatures.

order at 45 K, below this temperature a sine wave magnetic structure, similar to the one reported by Quezel *et al.*,[20] is found. At 16 K we obtain a propagation vector of $\delta=0.007$, 0.275, 0.0 with an amplitude of about $3.5\mu_B$. The phase between the atoms within one ab layer is 0.0775 or 28°. The plot of the Fig. 3 shows the indexation of the most important incommensurate diffraction peaks. Below 10 K the Tb moment ordering sets slowly in. It is of short range as deduced from the broadness of the diffraction peaks. This result nicely agrees with the dynamic behavior observed in the ac measurements at very low temperatures as will be shown below. The refined structural and magnetic data are shown in Table IV together with the results of all the other compounds studied by neutron diffraction.

The neutron-diffraction data of $Tb_{0.85}Ca_{0.15}MnO_3$ suggest the absence of magnetic long range order for this compound in agreement with the spin-glass behavior deduced from the susceptibility curves (see below). If a ferromagnetic component is included in the refinement at 2 K, a small value of

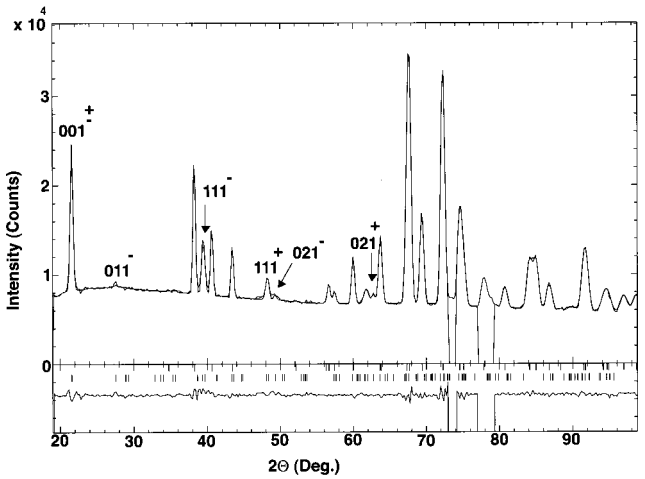

FIG. 3. Rietveld refinement of the neutron-diffraction pattern at 16 K for $TbMnO_3$. The difference between experimental and theoretical spectra is plotted at the bottom. The bars denoted the nuclear and magnetic reflections.

$0.7(0.2)\mu_B$ per Mn atom can be determined. However, a wavylike background which is indicative of remaining short-range correlations of the Tb sublattice renders the refinement less reliable, explaining the high value of the reliability factor (see Table IV).

Structural data for the sample with $x=0.33$ has been reported elsewhere.[21] This compound is magnetically inhomogeneous at low temperatures. The main phase is a spin-glass-like phase and small residual Mn moments are ordered in the *CE* type structure,[21] the Neel temperature (T_N) being 80 K for this AF phase.

$Tb_{0.5}Ca_{0.5}MnO_3$ also shows a *CE*-type magnetic ordering of the Mn moments as reported elsewhere.[14] In this type of structure, there are two different Mn sites and from the refinements, we determined the magnetic moment values to be 3.0 and $3.3\mu_B$. This sample develops a charge ordering at about[14] 300 K, see Fig. 2, whereas T_N is around 145 K.

Two magnetic phases are observed in $Tb_{0.35}Ca_{0.65}MnO_3$ at low temperatures. The ordering temperatures for both phases coincide or are very close to each other (T_N about 140 K). The first of the magnetic phases (about 35% of the total volume) is commensurate and best described as the superposition of two *C*-type sublattices with ferromagnetic chains along the [110] and [1–10] crystallographic directions, respectively. The second phase (65% of the total) has an incommensurate spiral structure with a propagation vector $\delta=(0.0\ 0.327\ 0.0)$. This incommensurate propagation vector is acting on a magnetic structure pattern, which is identical to the first commensurate magnetic phase. The plot of the Rietveld refinement is displayed in Fig. 4, a value of $2.4\mu_B$ is found for the Mn moment for both phases. A picture of the two magnetic structures can be found in Jirak *et al.*[5] who first found a similar mixing of magnetic phases in the related series $Pr_{1-x}Ca_xMnO_3$, for $x=0.7$.

A phase segregation is observed in $Tb_{0.15}Ca_{0.85}MnO_3$ at low temperatures. Additional diffraction peaks were first detected in the neutron diffractograms. In order to verify their origin, x-ray-diffraction measurements at low temperature were carried out. The refinements indicate the presence of two crystallographic phases at low temperatures. The main

TABLE IV. Refined fractional atomic positions, magnetic moment for Mn atoms, unit cell parameters and reliability factors obtained from neutron diffraction data for $Tb_{1-x}Ca_xMnO_3$ samples ($x=0$, 0.15, 0.33, 0.65, and 0.85) at 16 K for $x=0$ and at 2 K for the rest of samples. The Wyckoff positions in the *Pbnm* space group are: $(4c)$ for *R* (Tb/Ca) and O(1); $(4b)$ for Mn; $(8d)$ for O(2). The atomic positions in the $P2_1/m$ space group can easily be obtained by splitting the ones of the orthorhombic cell (considering the *Pnma* settings). Then, the Wyckoff positions for the monoclinic cell (unique axis *b*) are $(2e)$ for *R*, *R*′, O(1), and O(1)′, $(4f)$ for O(2) and O(2)′; $(2c)$ and $(2b)$ for Mn and Mn′, respectively.

					$x=0.85$	
	$x=0$	$x=0.15$	$x=0.33$	$x=0.65$	(21%)	(79%)
R:x	−0.0149(8)	−0.0143(16)	−0.0127(13)	−0.0066(14)	−0.0063(35)	0.0330(15)
(x')						0.5330(15)
y	0.0798(7)	0.0736(16)	0.0630(14)	0.0368(12)	0.0330(15)	1/4
z	1/4	1/4	1/4	1/4	1/4	−0.0063(35)
(z')						0.5063(35)
O(1):x	0.1053(8)	0.0955(17)	0.0900(13)	0.0800(13)	0.0628(20)	0.4822(15)
(x')						0.9822(15)
y	0.4668(7)	0.4698(7)	0.4727(12)	0.4868(12)	0.4822(15)	1/4
z	1/4	1/4	1/4	1/4	1/4	0.0623(20)
(z')						0.4372(20)
O(2):x	0.7039(7)	0.6988(14)	0.7042(9)	0.7128(8)	0.7174(16)	0.2937(13)
(x')						0.7937(13)
y	0.3259(6)	0.3132(13)	0.3013(9)	0.2924(7)	0.2937(13)	0.0394(9)
(y')						0.0394(9)
z	0.0515(4)	0.0494(12)	0.0448(7)	0.0378(5)	0.0394(9)	0.7174(16)
(z')						0.7826(16)
B_{overall}	0.1(1)	0.1(2)	0.3(2)	0.0(1)	0.1(5)	0.1(5)
Mn:μ_B	3.49(3)		1.6(3)	2.46(4)	2.7(1)	2.6(3)
			0.8(2)	2.44(4)		
a (Å)	5.3090(5)	5.3156(6)	5.3266(14)	5.3175(5)	5.2753(32)	5.3245(6)
b (Å)	5.8118(5)	5.6780(7)	5.5367(15)	5.3880(6)	5.3033(29)	7.4223(16)
c (Å)	7.3860(7)	7.4297(11)	7.4628(21)	7.4157(9)	7.4684(62)	5.2841(6)
β (deg.)						91.02(1)
R_p/R_{wp} (%)	1.6/2.1	2.7/3.5	2.8/4.1	2.4/3.1	2.5/4.1	
R_{Bragg} (%)	2.0	8.5	3.7	4.0	1.1	2.4

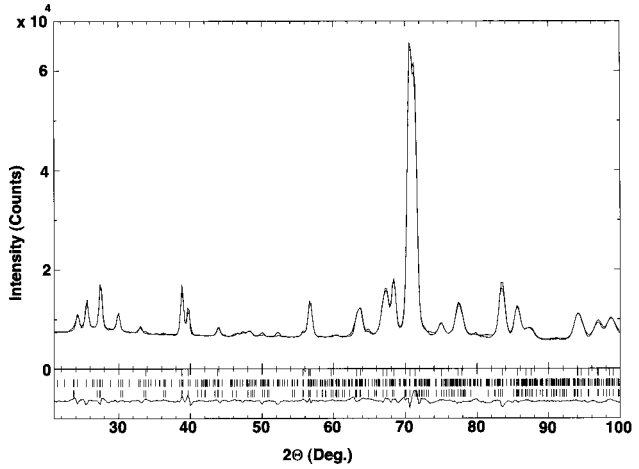

FIG. 4. Rietveld refinement of the neutron-diffraction pattern at 2 K for $Tb_{0.35}Ca_{0.65}MnO_3$. The difference between experimental and theoretical spectra is plotted at the bottom. The nuclear and magnetic reflections for the $2C$ type and the spiral magnetic structures are also shown.

phase is a monoclinic phase, space group $P2_1/m$, characteristic of systems that show the *C*-type magnetic arrangement.[12] The second phase has an orthorhombic unit cell, space group *Pbnm*, with a small orthorhombic distortion. The ratio between them is 85:15 at 80 K and 80:20 at 15 K. The x-ray refinement at 80 K is shown in Fig. 5 and Fig. 6 shows the refinement of the neutron-diffraction spectra at 2 K. The structural parameters obtained from the neutron-diffraction data at 2 K are reported in Table IV. Our results confirm the *C*-type magnetic structure for the monoclinic phase (79%) while the orthorhombic one (21%) shows a *G*-type magnetic arrangement with a ferromagnetic component. The temperature of the appearance of this ferromagnetic component nicely agrees with the anomaly in the thermal dependence of the lattice parameters (Fig. 2) and with the sharp peak seen in the ac susceptibility measurement (see below). Figure 7 shows the thermal evolution of the lattice parameters of the two individual phases as obtained from the neutron diffractograms. At room temperature, a single phase (*Pnma*) accounts for the whole pattern while at about 130 K a second orthorhombic phase, *G*-type magnetic and with different lattice constants, develops out of the original orthorhombic mother phase. The mother phase itself becomes as

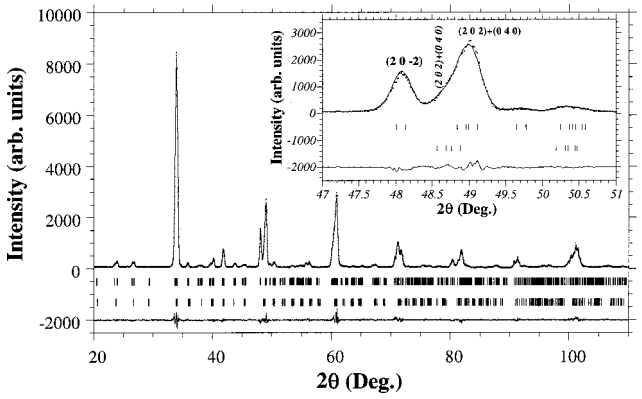

FIG. 5. The x-ray pattern (dots) and best fit (line) at 80 K for $Tb_{0.15}Ca_{0.85}MnO_3$. The difference between experimental and theoretical fit is plotted at the bottom. The bars denote the allowed Bragg reflections for the monoclinic and orthorhombic unit cells. Inset: Detail of the x-ray pattern showing both, the monoclinic splitting (horizontal index) and the contribution from the secondary phase (vertical index).

well magnetic but at slightly lower temperatures. This magnetic transition coincides with the nuclear phase transition to the monoclinic unit cell ($P2_1/m$). The large variation of the lattice parameters and of the monoclinic angle at this transition can be seen in Fig. 7. This kind of phase segregation was predicted in the past[3] and it has been observed in related compounds such as Sm-based manganites.[22]

3. Magnetic susceptibility

Let us now focus on the macroscopical magnetic properties of the series, which can roughly be divided in three regions depending on the x value. Figure 8(a) shows the initial ac susceptibility for $x \leqslant 0.3$ samples up to 150 K. A peak is observed for these samples at low temperatures ($T < 50$ K) and both, the temperature and magnitude of the peak increase with increasing Ca content. This behavior points to the enhancement of the ferromagnetic interactions. The susceptibility curve of $TbMnO_3$ peaks at 9 K where neutron-diffraction detected the onset of the ordering of localized Tb^{+3} moments. However, some differences can be noticed between the undoped sample $TbMnO_3$, and the rest of the series with $x \leqslant 0.33$. The doped samples show a dynamic behavior in the peak characteristic of a spin-glass system as reported[15] for $x = 0.33$. The frequency dependence of the freezing temperature T_f (cusp of the peak), for $Tb_{0.85}Ca_{0.15}MnO_3$ is displayed in Fig. 9. It is clear that T_f increases with increasing frequency of the ac field. The in-phase component χ' shows the expected diminution of the cusp value as the frequency increases. The out-of-phase component χ'' (absorption), also exhibits a peak at temperature slightly lower than χ'. This peak is also shifted to high temperatures by increasing the frequency of the ac field but the cusp value is now increased. These results might suggest that the spin-glass behavior shown by this compound be of type A glass.[23] Similar results were obtained for $x \leqslant 0.33$ samples. The origin for this spin-glass behavior is thought to lie in the competitive magnetic interactions shown by this family of compounds. It is well known that structural distortion weakens the F interactions between Mn^{3+}-Mn^{4+} ions (double exchange) and, below a critical ⟨Mn-O-Mn⟩ value, long-range ferromagnetism is not achieved. Instead, isolated ferromagnetic clusters appear as has been detected by several

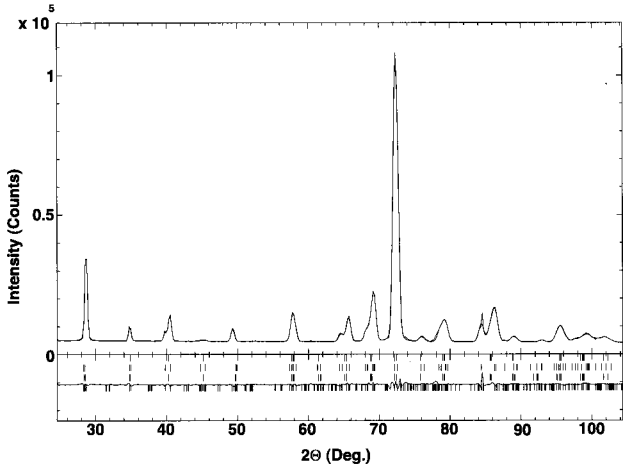

FIG. 6. Rietveld refinement of the neutron-diffraction pattern at 2 K for $Tb_{0.15}Ca_{0.85}MnO_3$. The difference between experimental and theoretical spectra is plotted at the bottom. The nuclear (orthorhombic and monoclinic) and magnetic reflections (G and C types) are also shown.

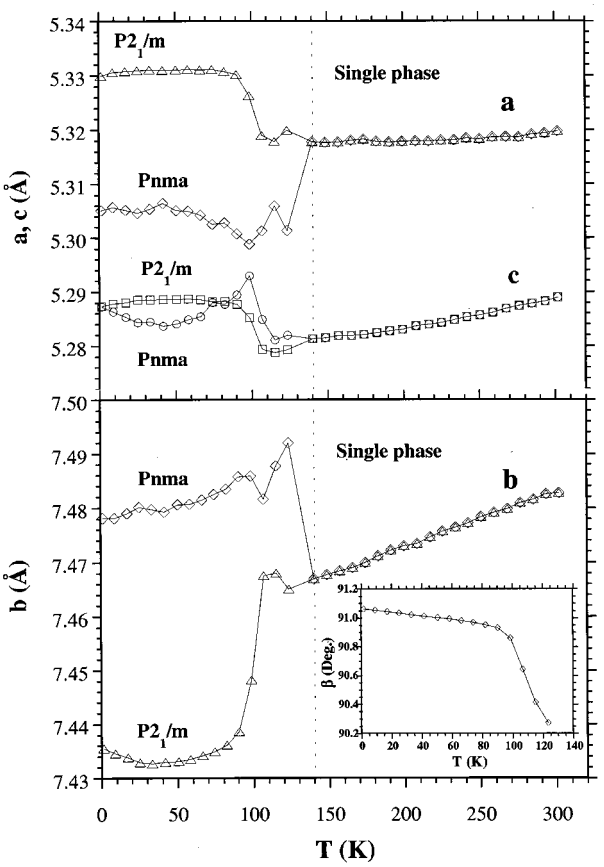

FIG. 7. Thermal evolution of the lattice parameters for $Tb_{0.15}Ca_{0.85}MnO_3$. The orthorhombic and monoclinic unit cell parameters are indicated in the plot. Pnma settings have been used for the orthorhombic structure to have a direct comparison with the monoclinic one. Inset: Thermal evolution of the β angle of the monoclinic phase.

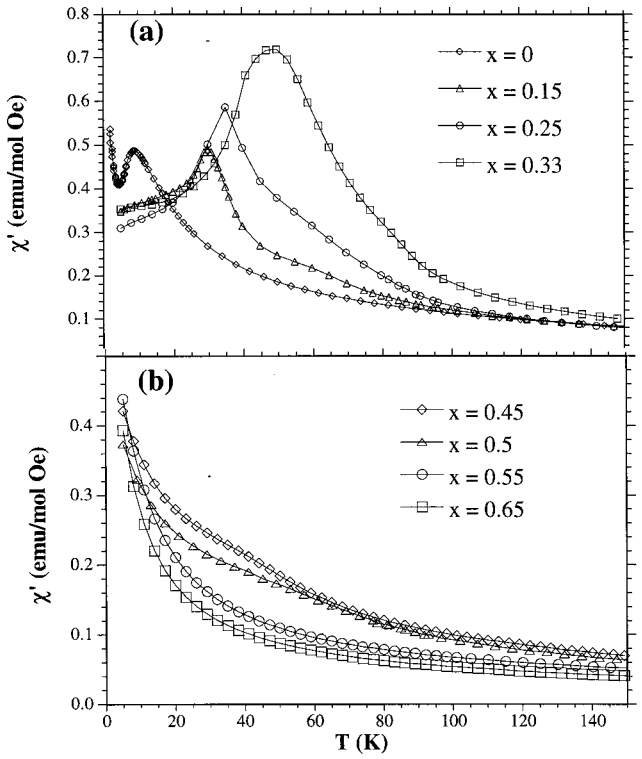

FIG. 8. Thermal dependence of the initial ac susceptibility curves for $Tb_{1-x}Ca_xMnO_3$ samples, (a) $0 \leqslant x \leqslant 0.33$, (b) $0.45 \leqslant x \leqslant 0.65$. The oscillating magnetic field has an amplitude of 4.5 Oe and a frequency of 12 Hz.

techniques such as SANS.[24] The samples studied in this work evidence a large structural distortion and low ⟨Mn-O-Mn⟩ values (see Table III). Accordingly, the spin-glass behavior can be ascribed to the existence of these ferromagnetic clusters. Recently, it has been proposed that a large size mismatch at the cation size (σ^2) favors the spin-glass state in manganites due to a random magnetic anisotropy.[25] Our results agree with this work because the value of σ^2 in nonnegligible for samples showing spin-glass behavior.

The undoped sample $TbMnO_3$ does not show dynamic behavior at the peak but at lower temperatures. Below the peak, there is an additional increase of the paramagnetic signal that depends on the frequency of the ac field, better noticed in the out-of phase component, see Fig. 9. This feature must be related to the Tb sublattice short range ordering as observed in neutron diffraction patterns below 10 K.

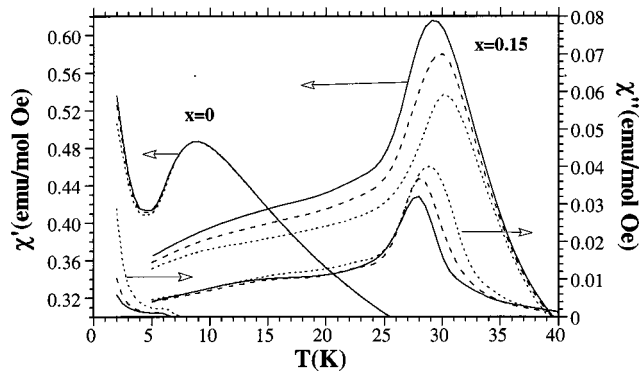

FIG. 9. Thermal dependence of the ac magnetic susceptibility for $TbMnO_3$ and $Tb_{0.85}Ca_{0.15}MnO_3$ samples at 1.2 (solid line), 12 (broken line), and 120 Hz (dotted line). The amplitude of the magnetic excitation field was 4.5 Oe.

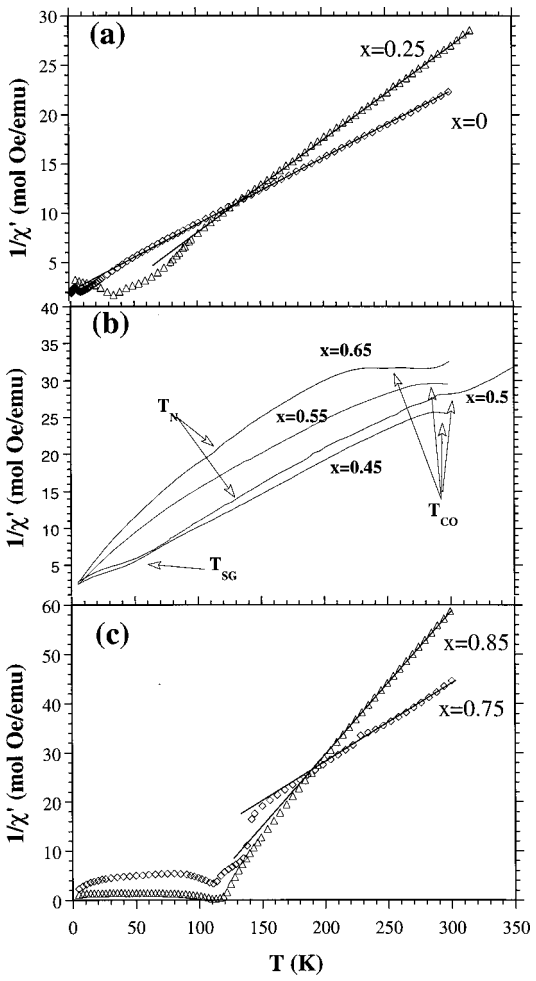

FIG. 10. The inverse of the magnetic susceptibility versus temperature for selected $Tb_{1-x}Ca_xMnO_3$ samples; (a) $x=0$ and $x=0.25$; (b) $0.45 \leqslant x \leqslant 0.6$, T_{CO}, T_N, and T_{SG} indicates the proposed temperatures for the different kind of transitions (charge ordering, AF and reminiscent spin glass); (c) $x=0.75$ and $x=0.85$. The straight lines are guides to eyes in order to show the linear behavior of some curves at high temperatures.

All of these samples ($x \leqslant 0.33$) follow a Curie-Weiss law at high temperatures. As example, plots of $1/\chi$ vs T for $x=0$ and $x=0.25$ are shown in Fig. 10(a). $TbMnO_3$ follows the Curie-Weiss law practically down to 45 K, temperature where the onset of the ordering of the Mn magnetic moments is observed by neutron diffraction. The other samples $0.15 \leqslant x \leqslant 0.33$, deviate from the Curie-Weiss law at higher temperatures (130–150 K). We have summarized the results from the fits to a Curie-Weiss law in Table V. In all cases, the effective magnetic moments obtained from these fits nicely agree with the expected ones[26] from $Mn^{3+}(4.9\mu_B)$, $Mn^{4+}(3.8\mu_B)$, and $Tb^{3+}(9.5\mu_B)$.

Samples with $0.45 < x < 0.65$ do not show apparent anomalies in their susceptibility curves, see Fig. 8(b). Only an apparent change of slope, better noticed in the $1/\chi$ plots, indicates the presence of phase transitions in these samples [see Fig. 10(b)]. None of these samples follows a Curie-Weiss behavior as can be observed in Fig. 10(b). The strong

TABLE V. Magnetic constants, experimental and theoretical—spin only for Mn ions and experimental value for Tb^{3+}—effective magnetic moments (Bohr magneton per formula unit) and fit range of the ac magnetic susceptibility data for $Tb_{1-x}Ca_xMnO_3$. The data were fitted to a conventional Curie-Weiss law $\chi = C/(T-\theta)$. Samples with $0.45 \leqslant x \leqslant 0.65$ do not follow this law.

Sample	C (emu K/mol)	θ (K)	$\mu_{\text{eff}}(\mu_B)$	Th. $\mu_{\text{eff}}(\mu_B)$	Fit range
$TbMnO_3$	15.0	−0.15	10.95	10.68	60–300 K
$Tb_{0.85}Ca_{0.15}MnO_3$	12.6	0	10.0	9.96	140–300 K
$Tb_{0.75}Ca_{0.25}MnO_3$	10.65	+0.1	9.25	9.45	140–300 K
$Tb_{0.67}Ca_{0.33}MnO_3$	9.85	+0.2	8.9	8.9	140–300 K
$Tb_{0.25}Ca_{0.75}MnO_3$	6.05	+0.7	6.95	6.3	200–300 K
$Tb_{0.15}Ca_{0.85}MnO_3$	3.38	+8.5	5.2	5.4	180–300 K
$Tb_{0.05}Ca_{0.95}MnO_3$	2.57	+1	4.4	4.4	160–300 K
$CaMnO_3$	2.26	−89	4.2	3.8	160–300 K

change of the slope observed at high temperatures is ascribed to the charge ordering transition[14] and they are also related to the sudden jump observed in the lattice parameters [compare Figs. 2 and 10(b) for $x=0.5$ and $x=0.65$; there is a relationship between the broadness in the change of both, the lattice parameters and the slope of $1/\chi$]. In addition, $x=0.5$ and $x=0.45$ show small anomalies at low temperatures, probably they arise from the formation of minority spin-glass phases similar to the ones present in samples with $x<0.45$.

Samples with $x>0.75$ show magnetic anomalies around 110–140 K distinctive of long-range ordering as can be observed in Fig. 11. All of these samples follow a Curie Weiss law at higher temperatures [see Fig. 10(c)] and the effective magnetic moments agree reasonably with the expected ones from the addition of localized moments of Tb^{3+}, Mn^{3+}, and Mn^{4+}. The magnetic anomalies observed in this range of compositions suggest again a complex magnetism as evidenced already in the neutron study for $x=0.85$. As explained above, a phase segregation takes place at low temperatures in this sample. The susceptibility curve shows a sharp peak (better noticed in the inset of Fig. 11) at temperatures where AF order takes place for both phases (see above). This peak is typical of weak ferromagnetism in agreement with neutron-diffraction results for this sample that shows a ferromagnetic component in the minority orthorhombic phase. A similar peak in the susceptibility curves has been reported[22] for the $Sm_{0.15}Ca_{0.85}MnO_3$ compound. The sample with $x=0.75$ shows two anomalies in the ac susceptibility curve. They can be ascribed to both transitions, a charge ordering and an AF ordering, developed practically at the same temperature in related $R_{1/4}Ca_{3/4}MnO_3$ compounds.[12] However, a phase segregation of this sample at low temperatures can not be neglected. $CaMnO_3$ shows an anomaly at 120 K that agrees with the AF ordering (G type) proposed for this compound.[2,6,12] Finally, the sample with $x=0.95$ exhibits a peak at 110 K that can be related to a long range AF ordering similar to the undoped $CaMnO_3$. However, the magnetic behavior is different below this temperature presenting a F component. It must be related to either a canting of the AF structure due to the presence of Mn^{3+} ions or to the appearance of cluster-glass regions as noticed in related compounds at similar doping ratio.[12]

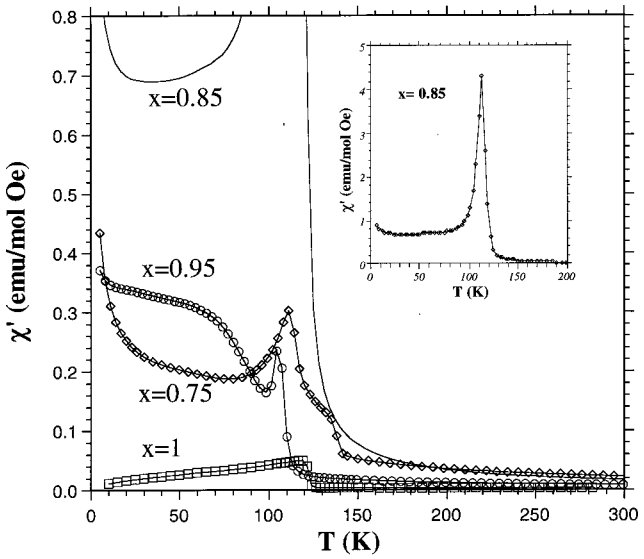

FIG. 11. Thermal dependence of the initial ac susceptibility curves for $Tb_{1-x}Ca_xMnO_3$ samples, $0.75 \leqslant x \leqslant 1$. The oscillating magnetic field has an amplitude of 4.5 Oe and a frequency of 12 Hz. Inset: Detail showing the sharp peak of the magnetic transition for $x=0.85$ sample.

IV. DISCUSSION

The main factors that control the magnetic coupling in this system are supposed to be the Mn-O-Mn superexchange[27] and the double exchange.[1] The former leads to AF interactions between pairs of Mn^{3+}-Mn^{3+} and Mn^{4+}-Mn^{4+}. The latter leads to F interactions between Mn^{3+}-Mn^{4+} by hopping of the e_g electron. One consequence of the small size of Tb^{3+} is the large tilting of the MnO_6 octahedra. Therefore, there is a decrease in the $\langle$Mn-O-Mn$\rangle$ bond angle and consequently, in the effective one-electron bandwidth[27,28] $W(W \approx \cos[180° - \langle \text{Mn-O-Mn} \rangle]/d_{\text{Mn-O}}^{3.5})$. This leads to a weakening of the F interactions and instead of developing a truly ferromagnetic state, as in La-based compounds, the system becomes a cluster glass for $0.15 \leqslant x \leqslant 0.33$. In addition, AF ordered regions are observed for $x=0.33$. The low value of the $\langle$Mn-O-Mn$\rangle$ bond angle reduces as well the AF superexchange interaction[29] and $TbMnO_3$ develops a long-range AF ordering at temperatures quite lower than related compounds such as $LaMnO_3$ or $PrMnO_3$. Furthermore, the magnetic ground state is incommensurate for $TbMnO_3$ while an A-type structure is shown by other $RMnO_3$ compounds, with R being a light rare earth.[1,17] Both,

a static Jahn-Teller effect and an *A*-type magnetic structure are considered evidence of orbital ordering for $R\mathrm{MnO_3}$ in agreement with superexchange interaction rules.[27] The departures of ⟨Mn-O-Mn⟩ from 180° strongly weaken the superexchange interaction between e_g orbitals and introduce overlap between t_{2g} orbitals on one cation and e_g orbitals on the other. It is thought that there is a critical angle around 135° where the latter interaction becomes preponderant.[27] Although there are some Mn compounds ($\mathrm{MnF_3}$) with ⟨Mn-O-Mn⟩ = 145° where the *A*-type structure is preserved, competitive magnetic interactions can be expected for $\mathrm{TbMnO_3}$ and it could provide a suitable explanation for the incommensurate structure.

For higher values of *x*, the charge ordered state is stabilized by the large lattice distortion and it appears close to room temperature for $0.45 \leqslant x \leqslant 065$. As recently shown by Vanitha *et al.*,[30] in manganites with $\mathrm{Mn^{3+}/Mn^{4+}} = 1$, T_{CO} increases as the average cation size decreases but it is not affected by the cation size mismatch. The low average cation size in this series explains the high T_{CO} we observe.

The magnetic ground state for $x > 0.65$ is inhomogeneous and it is a hallmark of competitive interactions among different lattice, charge and orbital degrees of freedom. The T_N for Tb-based samples are lower than those obtained for the equivalent La or Pr-based compounds,[5–6] but this difference decreases, as expected, as the Ca content increases. In addition, the kinds of AF structures found in the $\mathrm{Tb_{1-x}Ca_xMnO_3}$ series for $x \geqslant 0.5$ are similar to the ones reported for related systems with lighter rare earth atoms[2,5] but more complex magnetic behavior is observed. Finally, the phase segregation observed at low temperatures for $\mathrm{Tb_{0.15}Ca_{0.85}MnO_3}$ has also been noticed[22] in the related $\mathrm{Sm_{0.15}Ca_{0.85}MnO_3}$ compound.

V. CONCLUSIONS

The magnetic properties of $\mathrm{Tb_{1-x}Ca_xMnO_3}$ samples have been characterized by means of neutron-diffraction study and ac susceptibility measurements. The Tb-rich samples present a large structural distortion. This feature explains the insulator behavior of these samples and influences the magnetic properties of the series. The magnetic ground state of $\mathrm{TbMnO_3}$ is incommensurate and quite different from the related $R\mathrm{MnO_3}$ compounds. As the Ca content increases, the ferromagnetic interactions are reinforced but long-range *F* ordering is not achieved. Both features are related to the low $\mathrm{Tb^{3+}}$ ion size and the strong $\mathrm{MnO_6}$ octahedron distortion. This distortion is larger in this series than in the $\mathrm{La_{1-x}Ca_xMnO_3}$ series for corresponding values of *x*. Samples with $x \geqslant 0.5$ exhibit an AF ground state, which is mostly magnetically inhomogeneous. Moreover, for $x = 0.85$ a phase segregation is observed. Samples around $x = 0.5$ are charge ordered at high temperatures. This effect is enhanced by the narrow one-electron bandwidth of these compounds.

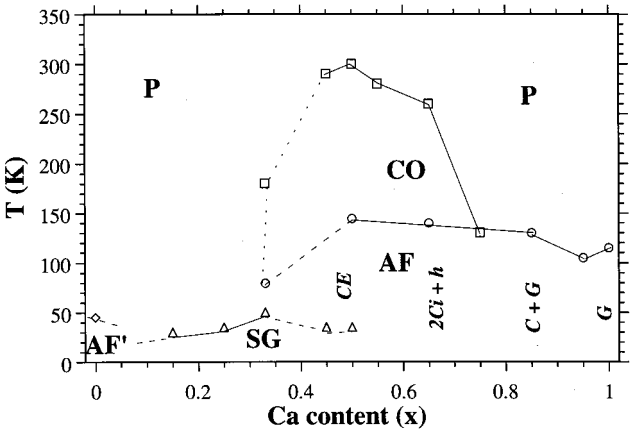

FIG. 12. Magnetic phase diagram of the $\mathrm{Tb_{1-x}Ca_xMnO_3}$ series. *P* stands for paramagnetic, SG for spin-glass-like, CO for charge-ordering, AF′ and AF for antiferromagnetic (incommensurate in the first case). The vertical letters indicate the different magnetic structures found in this work. The dotted lines are proposed boundary regions taking into account secondary phases.

According to both, the neutron-diffraction study and the ac susceptibility measurements, a preliminary phase diagram for the $\mathrm{Tb_{1-x}Ca_xMnO_3}$ series is proposed in Fig. 12. Further studies would be necessary in order to determine the exact composition range where the different magnetic structures are stable.

ACKNOWLEDGMENTS

This work has been supported by the Spanish C.I.C.Y.T. Projects No. MAT99-0847 and MAT99-1063-C04-01.

[1] C. Zener, Phys. Rev. **82**, 403 (1951).
[2] J. E. O. Wollan and W. C. Koehler, Phys. Rev. **100**, 545 (1955).
[3] J. B. Goodenough, Phys. Rev. **100**, 564 (1955).
[4] For a recent review see J. M. D. Coey, M. Viret, and S. Von Molnar, Adv. Phys. **48**, 167 (1999).
[5] Z. Jirák, S. Kupricka, Z. Simsa, M. Dlouhá, and S. Vratislav, J. Magn. Magn. Mater. **53**, 153 (1985).
[6] C. N. R. Rao, A. K. Cheetham, and R. Mahesh, Chem. Mater. **8**, 2421 (1996); B. Raveau, A. Maignan, C. Martin, and M. Hervieu, *ibid.* **10**, 2641 (1998).
[7] R. Kajimoto, H. Yoshizawa, H. Kawano, H. Kuwahara, Y. Tokura, K. Ohayama, and M. Ohashi, Phys. Rev. B **60**, 9506 (1999).
[8] M. R. Ibarra, P. A. Algarabel, C. Marquina, J. Blasco, and J. García, Phys. Rev. Lett. **75**, 3541 (1995).
[9] A. Millis, P. B. Litlewood, and B. I. Shraiman, Phys. Rev. Lett. **74**, 5144 (1995).
[10] H. Y. Hwang, S-W. Cheong, P. G. Radaelli, M. Marezio, and B. Batlogg, Phys. Rev. Lett. **75**, 914 (1995).
[11] L. M. Rodriguez-Martinez and J. P. Attfield, Phys. Rev. B **54**, R15622 (1996); C. N. R. Rao, R. Mahesh, A. K. Raychaudhuri, and R. Mahendiran, J. Phys. Chem. Solids **59**, 487 (1998).
[12] C. Martin, A. Maignan, M. Hervieu, and B. Raveau, Phys. Rev. B **60**, 12 191 (1999).
[13] I. O. Troyanchuk, N. V. Samsonenko, G. Shimchak, and A. Nabyalek, Phys. Solid State **39**, 101 (1997).

[14] J. Blasco, J. García, J. M. de Teresa, M. R. Ibarra, J. Pérez, P. A. Algarabel, C. Marquina, and C. Ritter, J. Phys.: Condens. Matter **9**, 10 321 (1997).
[15] J. Blasco, J. García, J. M. de Teresa, M. R. Ibarra, P. A. Algarabel, and C. Marquina, J. Phys.: Condens. Matter **8**, 7427 (1996).
[16] J. Rodriguez-Carvajal, Physica B **192**, 55 (1993); J. Rodríguez-Carvajal and T. Roisnel, URL: http://www-llb.cea.fr/winplotr
[17] S. Quezel-Ambrunaz, Bull. Soc. Fr. Mineral. Cristallogr. **91**, 339 (1968).
[18] K. R. Poeppelmeier, M. E. Leonowicz, J. C. Scanlon, J. M. Longo, and W. B. Yelon, J. Solid State Chem. **45**, 71 (1982).
[19] R. D. Shannon, Acta Crystallogr., Sect. A: Cryst. Phys., Diffr., Theor. Gen. Crystallogr. **32**, 751 (1976).
[20] S. Quezel, F. Tcheou, J. Rossat-Mignod, G. Quezel, and E. Roudaut, Physica B **86–88**, 916 (1977).
[21] J. M. de Teresa, C. Ritter, M. R. Ibarra, P. A. Algarabel, J. L. García-Muñoz, J. Blasco, J. García, and C. Marquina, Phys. Rev. B **56**, 3317 (1997).
[22] C. Martin, A. Maignan, M. Hervieu, B. Raveau, Z. Jirák, A. Kurbakov, V. Trounov, G. André, and F. Bourée, J. Magn. Magn. Mater. **205**, 184 (1999); R. Mahendiran *et al.* (unpublished).
[23] C. Y. Huang, J. Magn. Magn. Mater. **51**, 1 (1985).
[24] J. M. De Teresa, M. R. Ibarra, J. García, J. Blasco, C. Ritter, P. Algarabel, C. Marquina, and A. del Mora, Phys. Rev. Lett. **76**, 3392 (1996).
[25] A. Maignan, C. Martin, G. Van Tendeloo, M. Hervieu, and B. Raveau, Phys. Rev. B **60**, 15 214 (1999).
[26] A. K. Cheetham and P. Day, *Solid State Chemistry: Techniques* (Oxford University Press, Oxford, 1987), pp. 135–7.
[27] J. B. Goodenough and J. M. Longo, in Landolt-Börnsten, edited by H. Hellwege, Tabellen New Series, Group III/4a (Springer-Verlag, Berlin, 1970), pp. 207–213.
[28] M. L. Medarde, J. Phys.: Condens. Matter **9**, 1679 (1997).
[29] D. Treves, M. Eibschütz, and P. Coppens, Phys. Lett. **18**, 216 (1965).
[30] P. V. Vanitha, P. N. Santhosh, R. S. Singh, C. N. R. Rao, and J. P. Attfield, Phys. Rev. B **59**, 13 539 (1999).